Pyrolysis temperature effect on the efficacy of biochar/CuNi composite catalysts for emerging pollutant degradation

Mengqi Tang, Arvind K Bhakta, Youssef Snoussi, Khouloud Jlassi, Mohamed El Garah, Mohamed Chehimi

Pyrolysis temperature effect on the efficacy of biochar/CuNi composites used to catalyze emerging contaminant degradation

Mengqi Tang[1,*], Arvind K. Bhakta[1], Youssef Snoussi[1], Khouloud Jlassi[2],
Mohamed El Garah[3,4], Mohamed M. Chehimi[1,*]

1 Université Paris Cité, CNRS, ITODYS (UMR 7086), Paris 75013, France
2 Center for Advanced Materials, Qatar University, Doha, 2713, Qatar
3 LASMIS, Antenne de Nogent – 52, Pôle Technologique de Sud – Champagne, 52800 Nogent, France
4 Nogent International Center for CVD Innovation (NICCI), LRC CEA-LASMIS, Pôle Technologique de Sud Champagne, 52800 Nogent, France

Abstract

Sugarcane pulp bagasse biochar (SCPBB) was produced through pyrolysis from 500 to 900 °C under a nitrogen atmosphere, and their SCPBB/CuNi composites was produced through wetness impregnation with copper and nickel salts followed by pyrolysis. The impact of pyrolysis temperature on SCPBB and SCPBB/CuNi for physic-chemical properties was evaluated. SEM images that spherical bimetallic CuNi nanoparticles were evenly dispersed on the surface of the biochar matrix, and the size of the nanoparticles increased with increasing temperature. In particular, when the pyrolysis temperature is higher than 700 °C, the nanoparticles on the surface exhibit novel structures that are partially embedded or completely enclosed within the porous biochar matrix. FT-IR ATR and Raman spectra proved that SCPBB materials contain abundant surface functional groups and carbonaceous structures, which were preserved by the introduction of metal nanoparticles.TGA demonstrated SCPBB-500 biochar started to lose mass quickly first, followed by SCPBB-700 and finally SCPBB-900, and the weight residues of SCPBB@CuNi increased by 30%-34% compared with SCPBB. In addition, the catalytic performance of the synthesized material was explored for the degradation of malachite green (MG) representing dye molecules, Amoxicillin(AMX) representing pharmaceuticals, and Methyl-parabens(MP) representing personal care products contaminants. Each SCPBB/CuNi sample showed catalytic degradation performance under Advanted oxidation processes(AOPs), among which the SCPBB/CuNi catalyst obtained by pyrolysis temperature 500 °C performed best. Hence, SCPBB/CuNi demonstrates promising potential as a multifunctional catalyst for diverse environmental pollutants in wastewater treatments.

Keywords: antibiotics, cosmetics, pharmaceuticals and personal care products (PPCPs), biochar, *Saccharum officinarum*, Fenton-like nanocatalyst.

Corresponding authors: MMC (mohamed.chehimi@cnrs.fr), MT (mengqi.tang@etu.u-paris.fr)

1. Introduction

Carbon-rich biochar-based materials obtained by thermochemical conversion of biomass, including agricultural waste and forestry residues, animal manures and municipal wastes, have become a very popular and far-reaching catalyst supports for environmental remediation[1,2]. Slow pyrolysis is a classical and potent process of slowly heating up and staying for a long time under an oxygen-free atmosphere to fabricate biochar with abundant aromatization structure, which imparts chemical and biological stability to biochar [3].

Sugarcane bagasse, a byproduct of the sugar processing industry, is a residue with a global annual production of approximately 180 million tons [4]. The raw sugarcane bagasse/pulp mainly consists of 32-45% cellulose, 20-32% hemicellulose, and 17-32% lignin [5]. This kind of fibrous and dry agricultural waste can be used as a promising substitute material. Pyrolysis temperature is an important parameter for the conversion of biomass such as sugarcane bagasse to biochar [6]. It has been reported that hemicellulose can be decomposed at lower pyrolysis temperature, around 220-315 °C, cellulose decomposes around 280-400 °C, whereas lignin requires temperatures as high as 900 °C to completely decompose[7,8]. Additionally, the pyrolysis temperature also influences the physicochemical characterization of biochar, such as morphology, carbonaceous structure, pore size, functional groups, and elemental composition.

Based on the previous experience of our research group, the loading of bimetallic nanoparticles could be a good choice for the carbonization process to obtain the biochar composites with porous structure[9-11]. It is noted that Cu-based nanoparticles are commonly regarded as excellent catalysts with great pH tolerance and low oxidation-reduction potential[12], whereas Ni-based nanoparticles with magnetic performance could remarkably decrease the leaching of Cu active sites [13]. Moreover, Ni nanoparticles also contribute to the formation of pore structure for biochar support[9]. Biochar loaded with bimetallic copper-nickel or silver-copper nanoparticles are remarkable composites for the removal of toxic organic dye molecules [10,14,15]. Pharmaceuticals and personal care products (PPCPs) are other emerging persistent environmental pollutants which could compromise the quality of natural water. Their bioaccumulation in aquatic organisms could result in humans intoxication upon consumption of contaminated fish or shellfish[16]. It follows that PPCPs require efficient degradation processes. In this context, advanced oxidation processes (AOPs) are promising for efficient pollutant degradation technology[17]. Many kinds of catalytic systems using biochar-supported catalysts have been developed in this regard, Rad et al. [18] synthesized carbon nanotube/biochar-based nanocomposites as a sonophotocatalyst for sonocatalytic degradation of rifadin reached 80.3 % via AOPs. Zhao et al. [19] designed a Fe-N/biochar system as catalytic particle electrodes in an electro-Fenton/H_2O_2 system for the decomplexation and removal of a model pollutant. Eltaweil et al. [20] investigated Fenton-like degradation % of doxycycline reached 86.9 % after 1 h with biochar/amine chitosan composite decorated with CuNi layered double hydroxide. As a continuation of our

previous research, the bimetallic/Fenton-like technologies as an efficient system has once again captured our attention, this process relies on the valence state change of transition metals, such as Fe, Co, Cu, Ni, Cr and Mn, [20,21].

In this study, sugarcane pulp biochar (SCPBB) and SCPBB/CuNi composites prepared at different pyrolysis temperatures (500, 700, and 900°C) and thoroughly investigated for their physicochemical properties and catalytic performances. Additionally, the possibility of potential degradation of various contaminants in aqueous solutions via Fenton-like reactions is provided, with target contaminants including Malachite green representing dye molecules, and emerging pollutants amoxicillin representing pharmaceuticals, and methyl-parabens representing personal care products contaminants. Malchite Green degradation has been investigated in our previous study on the nanocatalyst loading effect at 500 °C slow pyrolysis temperature [https://doi.org/10.1016/j.envres.2023.116232], and herein it is employed to characterize the biochar composite catalysts prepared under various pyrolysis temperature, using optimized CuNi loading. We take advantage of our wet impregnation strategy to prepare biochar/bimetallic nanocatalyst to interrogate their propensity to catalyze PPCPs, considered as emerging pollutants requiring urgent development of highly efficient mineralization catalysts.

2. Materials and methods

2.1. Biomass and Chemicals

The raw sugarcane bagasse material was obtained from local farms in Egypt. Sugarcane pulp bagasse (SCPB) after drying is secondary finely ground before use as biomass feedstock. Metal nitrate $Cu(NO_3)_2{\cdot}6H_2O$ and $Ni(NO_3)_2{\cdot}6H_2O$ was purchased from Aldrich and used as a precursor for impregnating biomass. Distilled water dissolved metal nitrates as an aqueous solution.

2.2. Synthesis of biochar materials

Firstly, the SCPB powder was added to $Cu(NO_3)_2{\cdot}6H_2O$ and $Ni(NO_3)_2{\cdot}6H_2O$ aqueous solutions with different molar masses. The molar ratios of SCPB and CuNi were 0.5mmol pyrolyses 500°, 700°, 900°, respectively. The biomass was wet impregnated and then dried overnight at 60 °C. Then, the samples were pyrolyzed in a tube furnace under N_2 atmosphere to 500 °C for 1 h (the heating rate of 20 °C min^{-1}). Finally, the catalyst was cooled to room temperature under the N_2 flow and collected. The biochar samples loaded with metal nanoparticles were labeled as SCPBB@CuNi-500, SCPBB@CuNi-700 and SCPBB@CuNi-900, respectively.

2.3. Materials characterization

The crystalline structure of the biochar compositea, as shown were determined by XRD in the $20° \leq 2\theta \leq 100°$ range, using a D8 Advance Bruker diffractometer (Cu Kα radiation). The XRD data were processed using Highscore Plus software.

X-ray photoelectron spectroscopy (XPS) spectra were acquired using a K Alpha+ apparatus (Thermo, East Grinsted, UK) to determine the different major chemical elements on the surface of the samples. The machine employs a mono Al K (source energy = 1486.6 eV) and a flood gun for charge compensation. Avantage software was used for acquisition and processing of the data. The pass energy was set at 80 eV for the narrow regions, and 200 eV to record the survey spectra.

Raman spectra analysis wascarried out on the composites to determine the carbon signature by a Horiba HR 800 instrument. The curve fitting of the Raman was processed using MagicPlot software.

The surface morphology was investigated using a Hitachi SU 8030 Scanning Electron Microscope (SEM). Transmission electron microscope imaging was performed using a TecnaiG220 (FEI, Hillsboro, OR, USA) fitted with an energy dispersive spectrometer (EDS).

Fourier transform infrared (FTIR) attenuated total reflection (ATR) spectroscopy analyses were performed on a NICOLET 8700 spectrometer.

Thermal gravimetric analyses (TGA), a Setaram Setsys Evolution model was utilized, operating under N_2 atmosphere with a temperature range of RT-900 °C and a heating rate of 20 °C/min.

2.4. Catalytic activity

Catalytic tests were conducted using a methodology similar to that we previously reported [9,14]. Biochar supported bimetallic nanoparticle SCPBB/CuNi prepared at various pyrolysis temperatures was employed as a catalyst for catalytic degradation of three target pollutants in wastewater, namely Malachite Green (dye), Amoxicillin (antibiotic, obtained from local pharmacy in Paris, “Pharmacie Grosicki”) and methyl-paraben (cosmetic). For each experiment, 5 mg of the biochar catalyst was introduced into a solution (20 mL, concentration: 20 mg/L). The addition of H_2O_2 triggered the Fenton-like degradation reaction of the organic pollutants. The suspension was filtered to determine the residual dye concentration, and UV-Vis spectrophotometry was employed at specific time intervals.

3. Results and Discussion

In this work, we targeted to investigate the pyrolysis temperature effect on the catalytic performance of biochar@CuNi. It is well-known that at 500 °C, the H/C ratio starts to be significantly low and thus one reaches a highly carbon-rich structure [https://doi.org/10.1038/srep22644]. During the pyrolysis of biomass at low temperature, tar is the main product formed [], while only a small amount of biochar is produced. When the pyrolysis temperature is 500°C, the biochar yield reaches the maximum. As the temperature increases from 500 °C, secondary cracking reactions occur and tar yield reduces during the pyrolysis process. Therefore, the pyrolysis region of 500-900°C was selected to further study. This has also been explained in the seaweed biochar pyrolysis process[10.1016/j.algal.2020.101900]. In this regime, and particularly under slow pyrolysis conditions, biochar is the main product [https://doi.org/10.3390/surfaces6020013], which is important in this work as it serves as support for the nanocatalysts. Temperature is also an important parameter controlling biochar textural properties [https://doi.org/10.1016/j.scitotenv.2020.144204], with an ideal 400-700 °C pyrolysis temperature range, as well as carbonization and graphitization [https://doi.org/10.1007/s42773-020-00056-0]. However, as we consider the pyrolysis of nanocatalyst precursor-impregnated biomass, the pyrolysis temperature effect on the final biochar composite catalyst is worth this comprehensive investigation.

3.1. Catalyst characterization

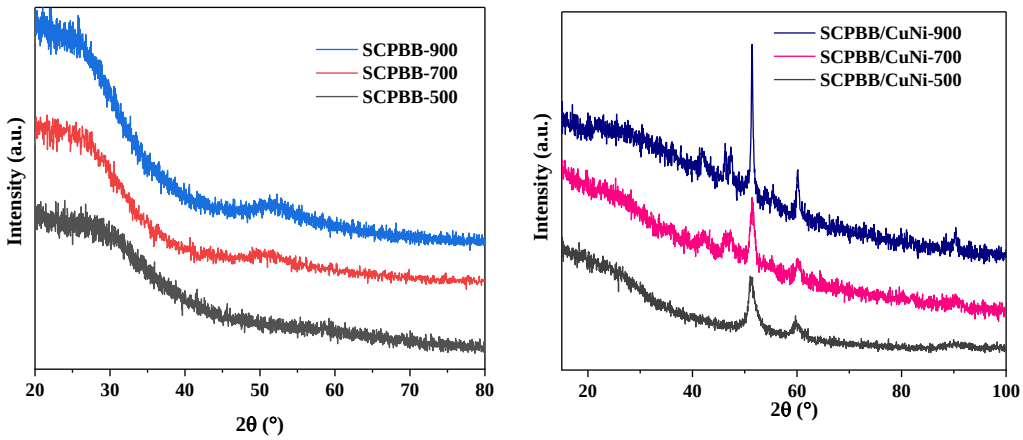

Fig. 1. XRD pattern of SCPBB biochar (a) and SCPBB/CuNi (b).

For pure SCPBB materials, Fig. 1a exhibits two broad diffraction peaks near 23° and 43°, attributed to the (002) plane and (100) plane of carbon, respectively, indicating that sugarcane pulp bagasse biomass converted to amorphous carbon under high-temperature pyrolysis[22]. The carbonaceous structural peaks observed at 51.3° for the high-temperature biochars SCPBB-700 and SCPBB-900 indicated the formation of slightly ordered biochars[23]. However, there are two typical peaks in SCPBB/CuNi composites at 51.3 ° and 60.0 °, which are indexed to (111) planes and (002) planes of copper nickel (ICSD No.98-062-8542), respectively. The diffraction peaks become sharper as increasing pyrolysis temperature, implying the high crystallinity of CuNi alloy successfully supported on biochar, as well indicated that smaller alloy particles merge into larger alloy particles on the surface[24].

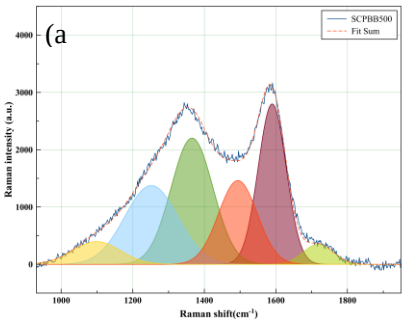

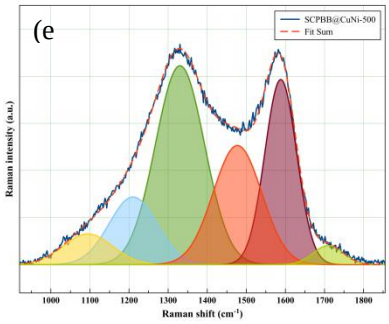

(f

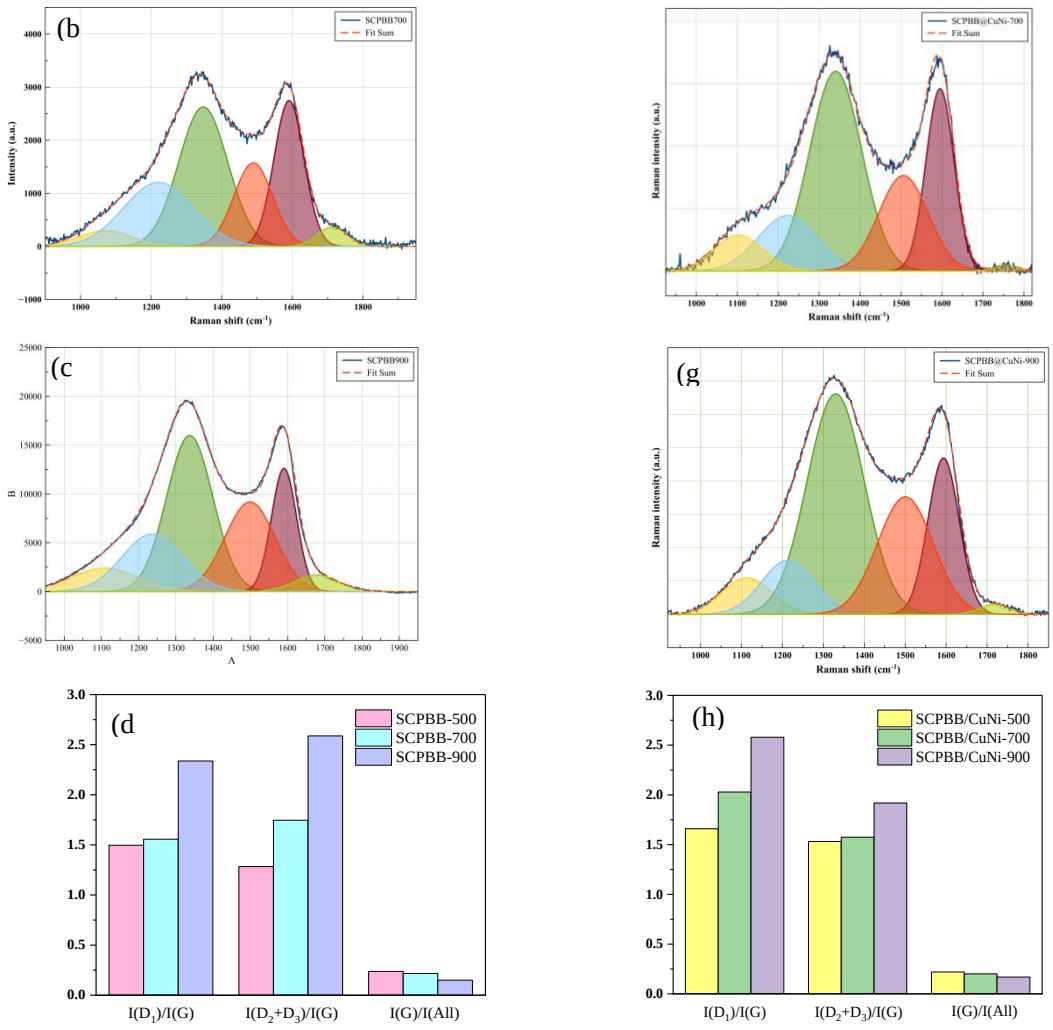

Fig. 2. Raman spectra of pure SCPBB(a-c) and SCPBB@CuNi(e-g), the Raman band area ratios of SCPBB(d) and SCPBB/CuNi(h).

Raman spectroscopy can identify both presence of graphite and amorphous carbon in these samples, which were fitted using Lorentzian and Gaussian functions for the background correction, different band height and integral areas measurements[25]. The Raman spectra of all biochar samples exhibit two strong peaks in the D_1 and G bands (Fig. 2). The D band around 1340-1370 cm^{-1} corresponds to the structural defects, while the G band at about 1580-1600 cm^{-1} corresponds to the graphite C=C bond[26].The D_2 (V-band, ~1500 cm−1) and D_3 bands (~1200 cm−1) are associated with amorphous carbon structure and mixed sp^2-sp^3 bonds, respectively[27]. Fig. 2(d) illustrates the related band area ratios for all biochars. The ratio $I(D_1)/I(G)$ have an inverse proportional correlation with the crystallite size[28], the lower $I(D_1)/I(G)$ suggests the average planar size of the graphite

microcrystals is higher[29]. Similarly, the $I(D_2+D_3)/I(G)$ ratio also increases as the pyrolyzed temperature increases, the condensed aromatic ring structures with defects and the presence of a significant amount of amorphous carbon in the SCPBB biochar[28]. Simultaneously, with the increase in pyrolysis temperature, and D peak shapes of biochars and their composites becomes narrower, which indicates a growing order of the carbon matrix during pyrolysis as non-crystallite carbon is decomposited/polymerized into larger molecules[30]. Interestingly, the Raman spectra of the bimetallic-impregnated biochar SCPBB/CuNi show similarities to those of pure biochar SCPBB, with a reduced $I(D_1)/I(G)$ ratio (Fig. 2(h)). This suggests the incorporation of the bimetallic nanoparticles enhances the uniformity of carbon structure, leading to a higher degree of graphitic carbon formation in the composite material[31].

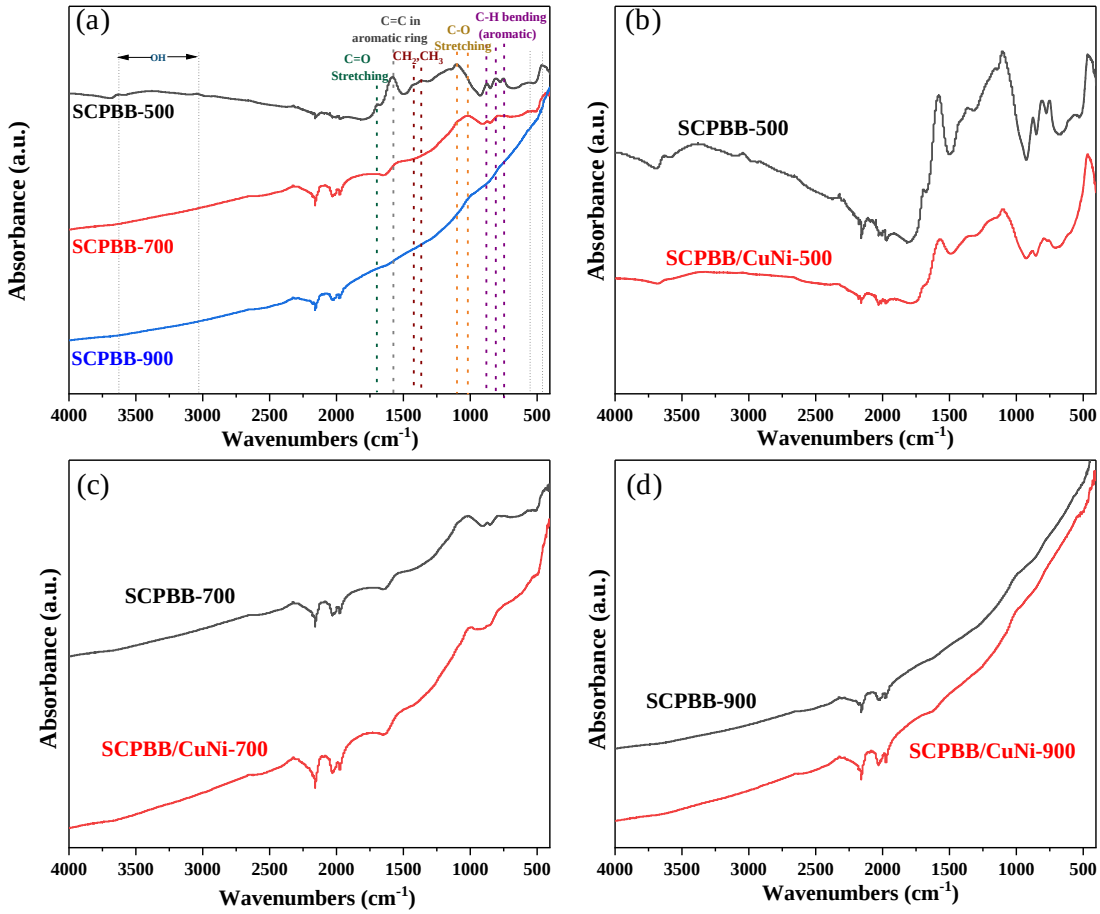

Fig. 3. FTIR-ATR spectra of pure biochar under different pyrolysis temperatures(a), SCPBB vs. SCPBB/CuNi under different pyrolysis temperatures(b-d).

The FTIR-ATR spectra illustrate the transformation of biochar under varying pyrolysis temperatures and the impact of metal nanoparticles in Fig. 3. Broad bands observed at 3100-3660 cm^{-1} and ~1700 cm^{-1} representing -OH and C=O stretching vibrations, which are attributed to dehydration and decarboxylation during pyrolysis[32,33]. The 2800-3000 cm^{-1} and ~1435 cm^{-1} regions represent aliphatic functional groups CH_3 and CH_2 stretching and deformation vibrations. The C=C, C=O for ketones and quinones occur in the region around 1600 cm^{-1} and aromatic C-H occurs between 885 - 750 cm^{-1}. The strong band at 1030 cm^{-1} is attributed to the C-O stretching of phenolic related to oxygenated functional groups of cellulose, hemicellulose, and methoxyl groups of lignin[33,34]. Strong aromatic C=C stretching vibration was observed in biochar produced at 500 °C, indicating the formation of aromatic structures in the biochar[32]. The vibrations of functional structures also persisted for pyrolysis temperature to 700°C. Meanwhile, as the pyrolysis temperature increases to 900°C, SCPBB shows a similar spectrum, but the intensity of its functional groups decreases. Remarkably, loading copper and nickel metal nanoparticles preserves almost all organic functional groups over biochar supports. It can be suggested that the pyrolysis temperature has a significant influence on the organic functional structure of biochar-based materials.

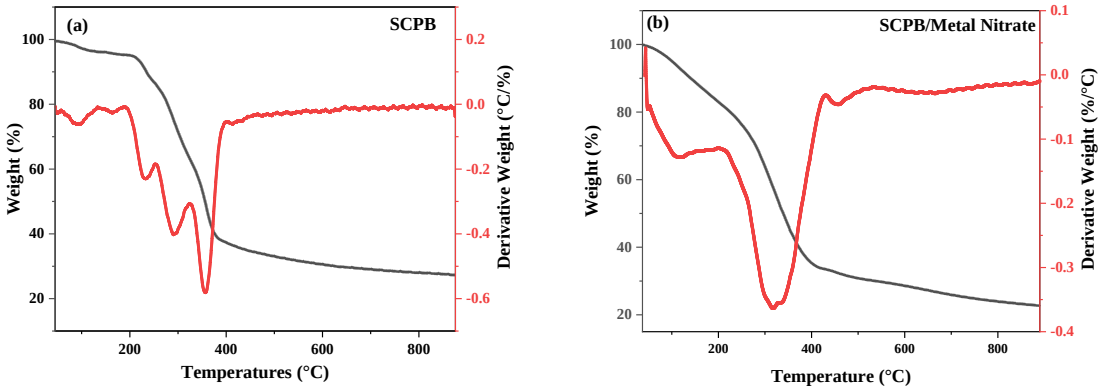

Fig. 4. TGA/DTG analyses of the sugarcane pulp bagasse(SCPB) and sugarcane pulp bagasse with metal nitrate salts.

The decomposition of sugarcane pulp bagasse and its wet-impregnated mixture with metal nitrate under a nitrogen atmosphere was studied by thermogravimetric analysis (TG), consistent with the conditions of pyrolysis synthesis. The TG/DTG curve shown in Fig. 4(a), the thermal degradation of SCPB is 4.6% mass loss between 40 °C and 189 °C, which is related to moisture loss and devolatilization [35]. The second weight loss stage of sugarcane bagasse begins at ~200 °C, with approximately 60% mass loss, and complete thermal degradation of holocellulose occurs at approximately 400 °C. This is a main weight loss stage associated to the sum of volatiles,

hemicellulose, cellulose and lignin thermal decomposition, respectively[36]. For the mixture of sugarcane pulp bagasse with $Cu(NO_3)_2 \cdot 6H_2O$ and $Ni(NO_3)_2 \cdot 6H_2O$, Fig. 4(b) can be clearly observed on the DTG curve that the first peak corresponds to the moisture from SCPB and bound water molecules from hydrated metal salts during wetness impregnation. This is followed by two overlapping peaks, hemicellulose (312 °C) and cellulose (333 °C), with the peak corresponding to lignin partially overlapping the other two peaks at 430°C -550°C [37]. A broader peak is observed, attributed to weight loss caused by lignin decomposition reactions[7].

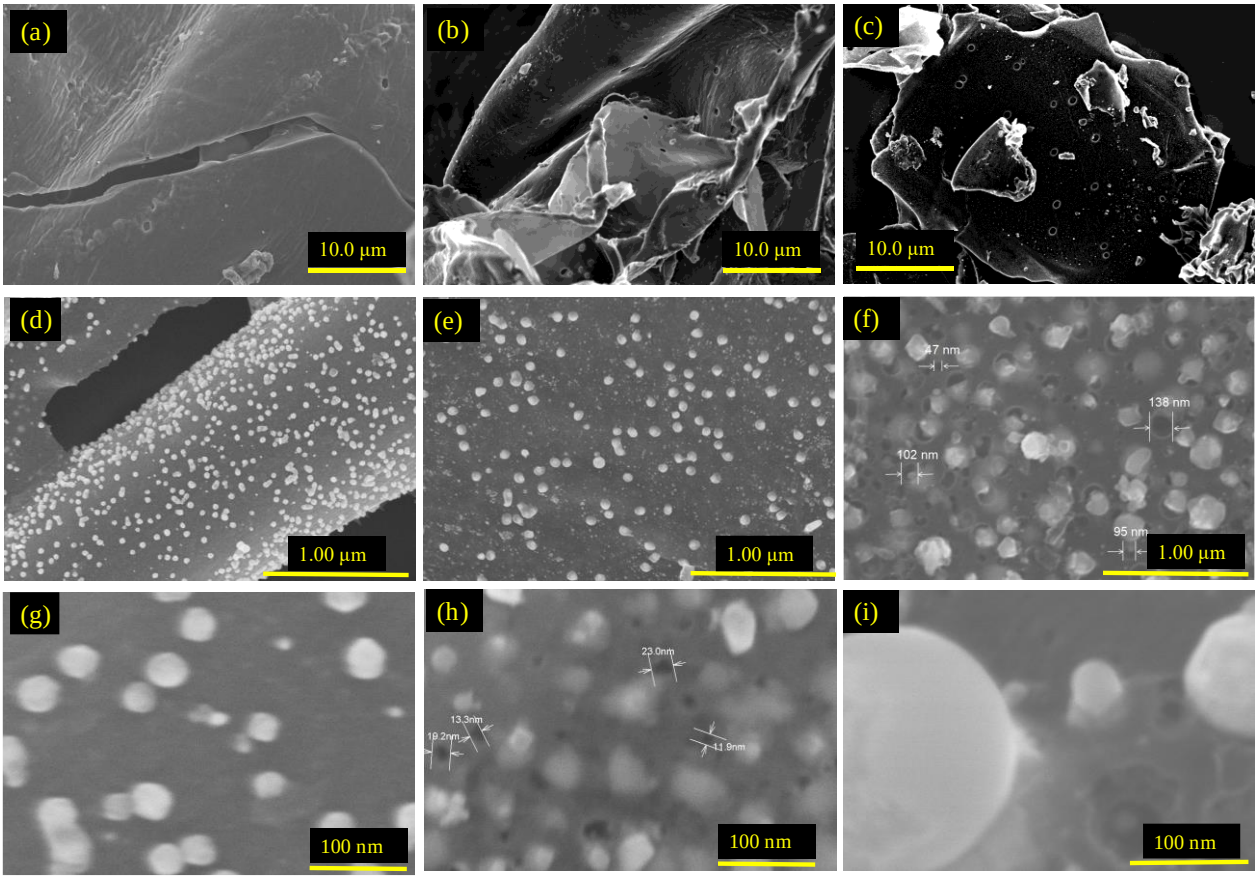

Fig. 5. SEM images of biochar: SCPBB-500 (a), SCPBB-700(b), SCPBB-900(c), thermal-treated CuNi-impregnated biochar composites: SCPBB/CuNi-500(d,g), SCPBB/CuNi-700(e,h) and SCPBB/CuNi-900(f,i).

SEM images of the SCPBB and SCPBB@CuNi at different pyrolysis temperatures are shown in Fig. 5. Pure SCPBB biochar had a smooth surface(Fig. 5 a-c), which makes it a good carrier and support. The loading of the bimetallic nanoparticles on biochar induced a cracked and porous structure (Fig. 5d-f). The CuNi alloy nanoparticles are spherical and evenly distributed on the biochar, and the particle size of CuNi nanoparticles obviously increases with the gradual increase of pyrolysis temperature, which is consistent with the XRD data.

Notably, SCPBB/CuNi-700 and SCPBB/CuNi-900 formed larger pores and channel structures due to release more volatile substances as raising pyrolysis temperature, and CuNi particles are either partially embedded or fully enclosed within the porous biochar matrix.

In the Fig. 6, particle size and shape were investigated through TEM images with micron-scale of biochar-based composites. It was observed that CuNi metal nanoparticles with spherical on the biochar matrix, the particle size distribution of 5-15 nm, 15-23 nm and 12-26 nm, the mean size of 11.68 nm, 18.23 nm and 18. 91 nm at pyrolysis temperatures of 500°C, 700°C and 900°C, respectively. These metal nanoparticles as alloys aggregated by the high surface energy and surface tension[38], and there are porous structures appeared in surfaces with pyrolysis temperature above 700 °C.

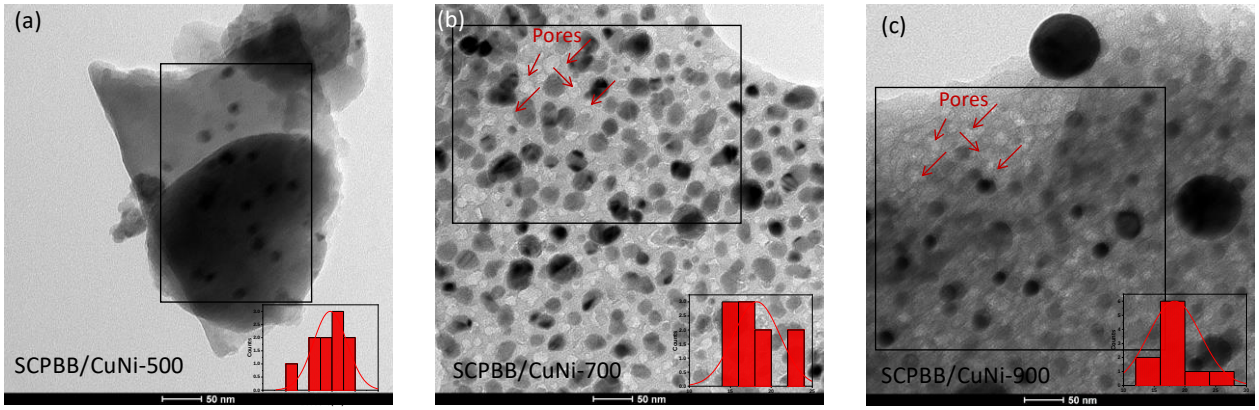

Fig. 6. TEM images of CuNi-impregnated biochar composites: SCPBB/CuNi-500 (a), SCPBB/CuNi-700(b) and SCPBB/CuNi-900(c).

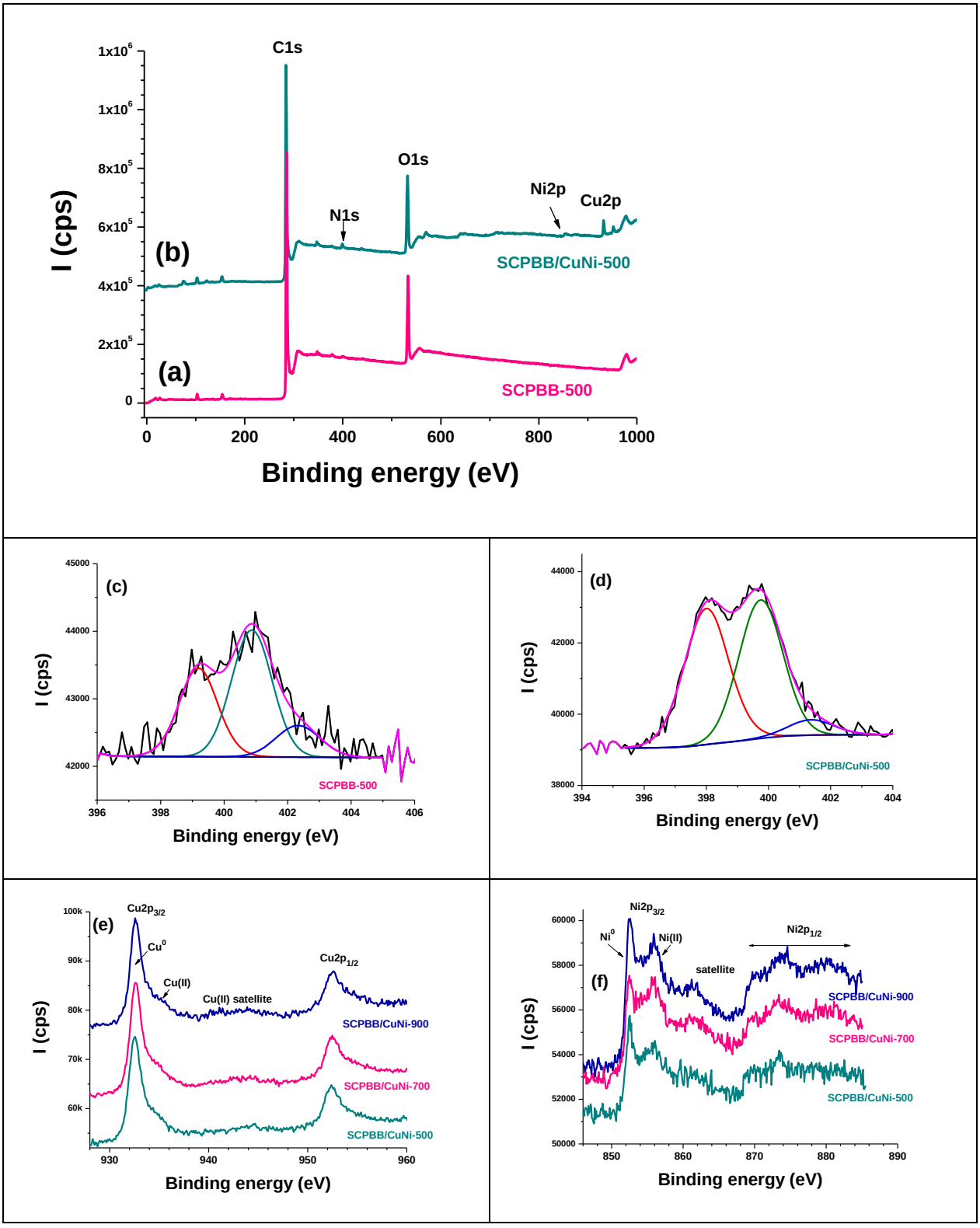
C1s
O1s
N1s
Ni2p
Cu2p
(b)
SCPBB/CuNi-500
(a)
SCPBB-500
I (cps)
Binding energy (eV)
(c)
SCPBB-500
(d)
SCPBB/CuNi-500
(e)
Cu2p3/2
Cu0
Cu(II)
Cu(II) satellite
Cu2p1/2
SCPBB/CuNi-900
SCPBB/CuNi-700
SCPBB/CuNi-500
(f)
Ni2p3/2
Ni0
Ni(II)
satellite
Ni2p1/2
SCPBB/CuNi-900
SCPBB/CuNi-700
SCPBB/CuNi-500

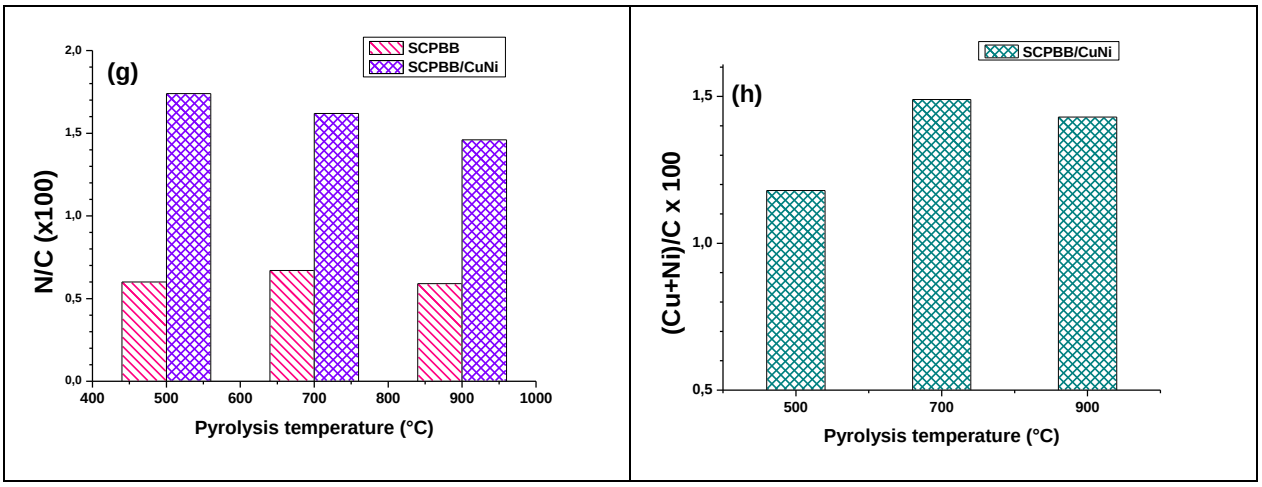

Fig. 7. XPS analysis of biochar samples: survey regions of SCPBB-500 (a) and SCPBB/CuNi-500, peak-fitted N1s from SCPBB-500 (c) and SCPBB/CuNi-500EM (d), Cu2p (e) and Ni2p (f) regions from SCPBB/CuNi samples; N/C atomic ratio (g), and (Cu+Ni)/C atomic ratio versus pyrolysis temperature.

XPS was used as a unique surface analytical technique to determine the surface chemical composition of bare and nanocatalyst-coated biochar samples. Figure 7 displays the survey regions of SCPBB/CuNi-500 (Figure 7b) and that of the same biochar, prepared without any catalyst (Figure 7a). The addition of copper and nickel specific peaks is clearly visible despite their low relative intensity, due to the dispersed nature of the CuNi nanoparticles instead of a continuous nanoparticle top layer. N1s is peak-fitted for both SCPBB-500 (Figure 7c) and SCPBB/CuNi-500 (Figure 7d) with three components assigned to pyridinic (398.5-399 eV), pyrrolic (400±0.5 eV), and graphitic (401.2±0.5 eV) nitrogen atoms, respectively. Concerning the SCPBB/CuNi materials, the contributions of the pyridinic, pyrrolic, and graphitic nitrogen types to the total N1s peak-area (47.2, 47.2, 5.6%), (40.3, 50.4, 9.3%), and (34.1, 52.4, 13.5%) for the pyrolysis temperature of 500, 700 and 900 °C.

All Cu2p regions do not seem to be affected by the pyrolysis temperature, and the Cu2p regions are dominated by the metallic state of copper ($Cu2p_{3/2}$ centred at ~932.4 eV), however with little oxidation evidenced by $Cu2p_{3/2}$ centred at ~934.7 eV and particularly by the broad satellite feature (940-948 eV). Nickel shows complex Ni2p spectrum showing the coexistence of nickel in both the metallic and the Ni(II) oxide states ($Ni2p_{3/2}$ centred at 852.5 and 856.0, respectively). The broad satellite region (860-868 eV) is consistent with Ni(II) oxidation state. There seems to be slightly more nickel oxide at 700 and 900 °C.

The N/C atomic ratio is plotted versus pyrolysis temperature for all samples (Figure 7g). It shows clearly that the wet impregnation affects the carbon structure, and the nitrogen containing heterocycles seem to withstand

elevated temperature. Yet, one can note a gradual decrease in the N/C ratio with increasing preparation temperature for the SCPBB/CuNi samples. For the SCPBB/CuNi samples, there is a slight increase in total metal to carbon atomic ratio as a result of the increasing of the pyrolysis temperature (Figure 7h); this is due to the elimination of carbon during the carbonization and the creation of the porous structure of the underlying biochar. Surprisingly, despite the impregnation of equal number of moles of copper and nickel ions, the Cu/Ni atomic ratio was found to be 2.1, 1.42 and 0.97 (nearly 1) for SCPBB/CuNi prepared at 500, 700 and 900 °C. Possibly, the bimetallic catalyst nanoparticles undergo segregation of copper to the outermost surface of the nanoparticles at lower pyrolysis temperature, and at 900 °C there could be more mobility of nickel yielding a Cu/Ni atomic ratio equal 1, matching the initial ratio during the wet impregnation process, prior to pyrolysis.

3.2. Catalytic application of SCPBB@CuNi

3.2.1. Removal of Malachite green dye

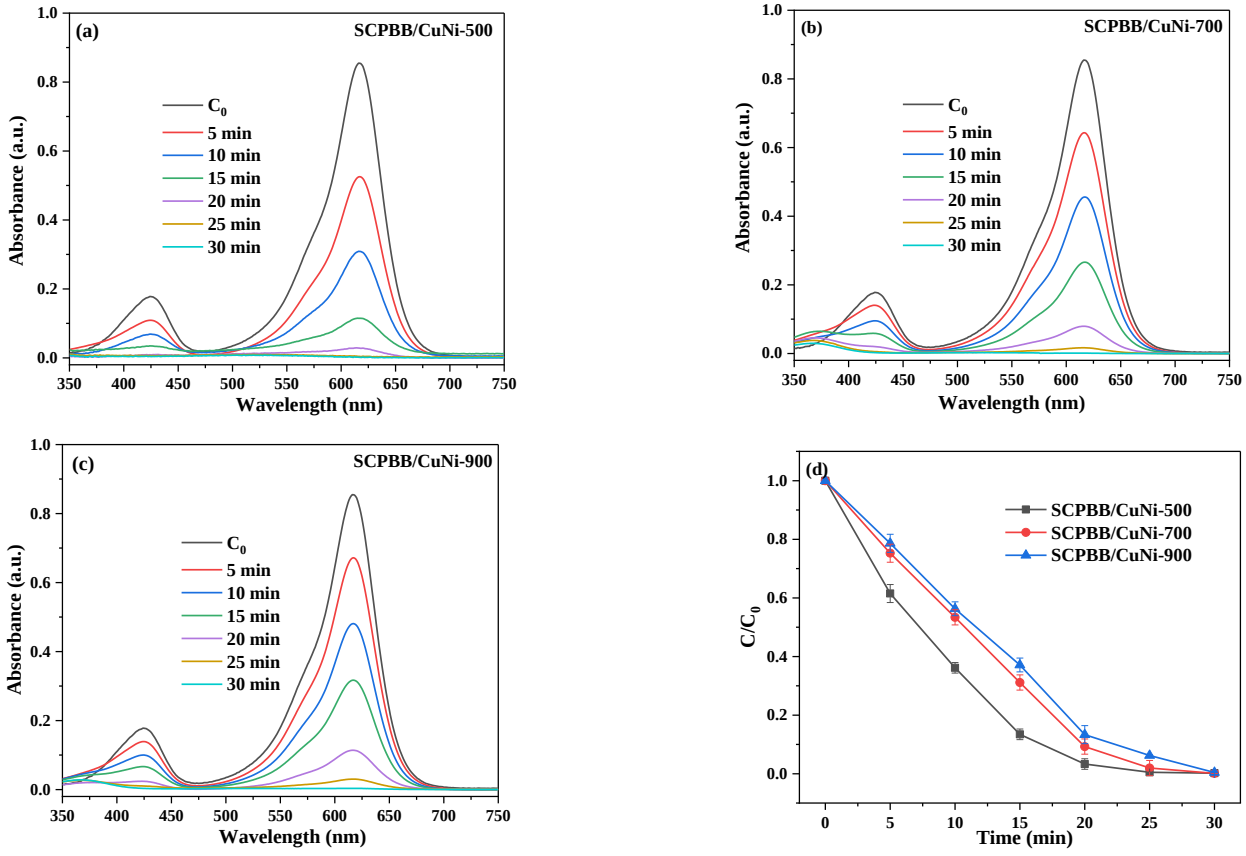

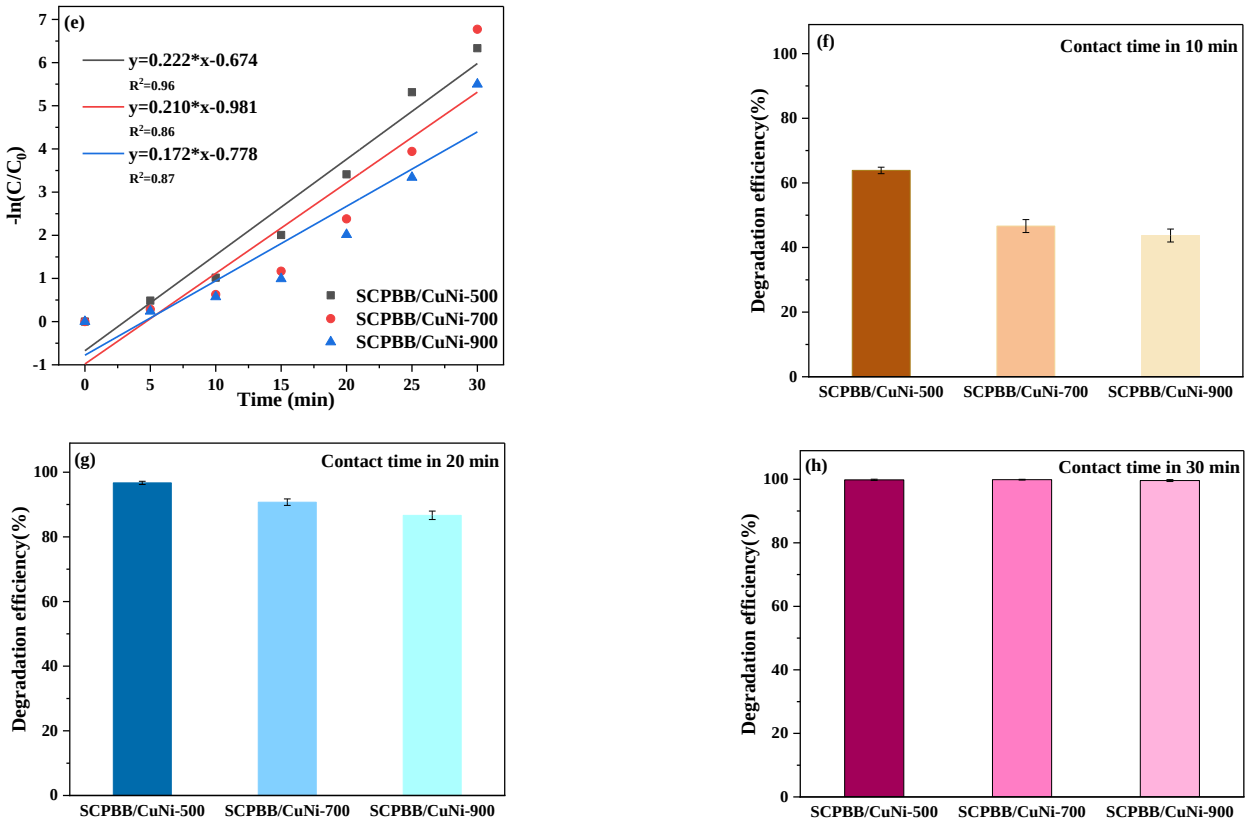

Fig. 8. Catalytic degradation of Malachite Green: UV-vis spectra using SCPBB/CuNi-500(a), SCPBB/CuNi-700(b), SCPBB/CuNi-900(c), C/C_0-vs-time plots(d), -ln (C/C_0)-vs-time plot(e), the corresponding removal % in 10 min(f), 20 min(g), 30 min(h).

SCPBB/CuNi composites with different pyrolysis temperatures, a range of heterogeneous catalysts, was assessed for its catalytic activity in degrading Malachite green (MG) dyes under the optimal experimental conditions reported previously. Spectral changes as shown in Fig. 8a-c; all SCPBB/CuNi catalysts achieved significant degradation efficiency in 30 min in the presence of H_2O_2.To assess the reaction rate, we conducted a study to estimate the degradation of MG over SCPBB/CuNi generated material as a function of reaction time. The degradation kinetics were quantitatively evaluated using the pseudo-first-order model, $-Ln(C/C_0) = kt$, where 'C' represents the dye concentration at time 't', 'C_0' is the initial dye concentration, and 'k' is the rate constant(min^{-1}). The ranking of rate constant "k" for MG degradation by these catalysts is as follows, from highest to lowest: SCPBB/CuNi-500 > SCPBB/CuNi-700 > SCPBB/CuNi-900. Moreover, it can be seen from C/C_0 that SCPBB/CuNi-500 exhibited higher catalytic efficiency, with 64% in 10 min and approximately 96% in 20 min.

In contrast, SCPBB/CuNi-700 and SCPBB/CuNi-900 showed slower degradation rates of 47 and 43%, respectively, within the first 10 min but all catalysts were able to completely remove the dye molecule within 30 min.

3.2.2. Removal of Amoxicillin

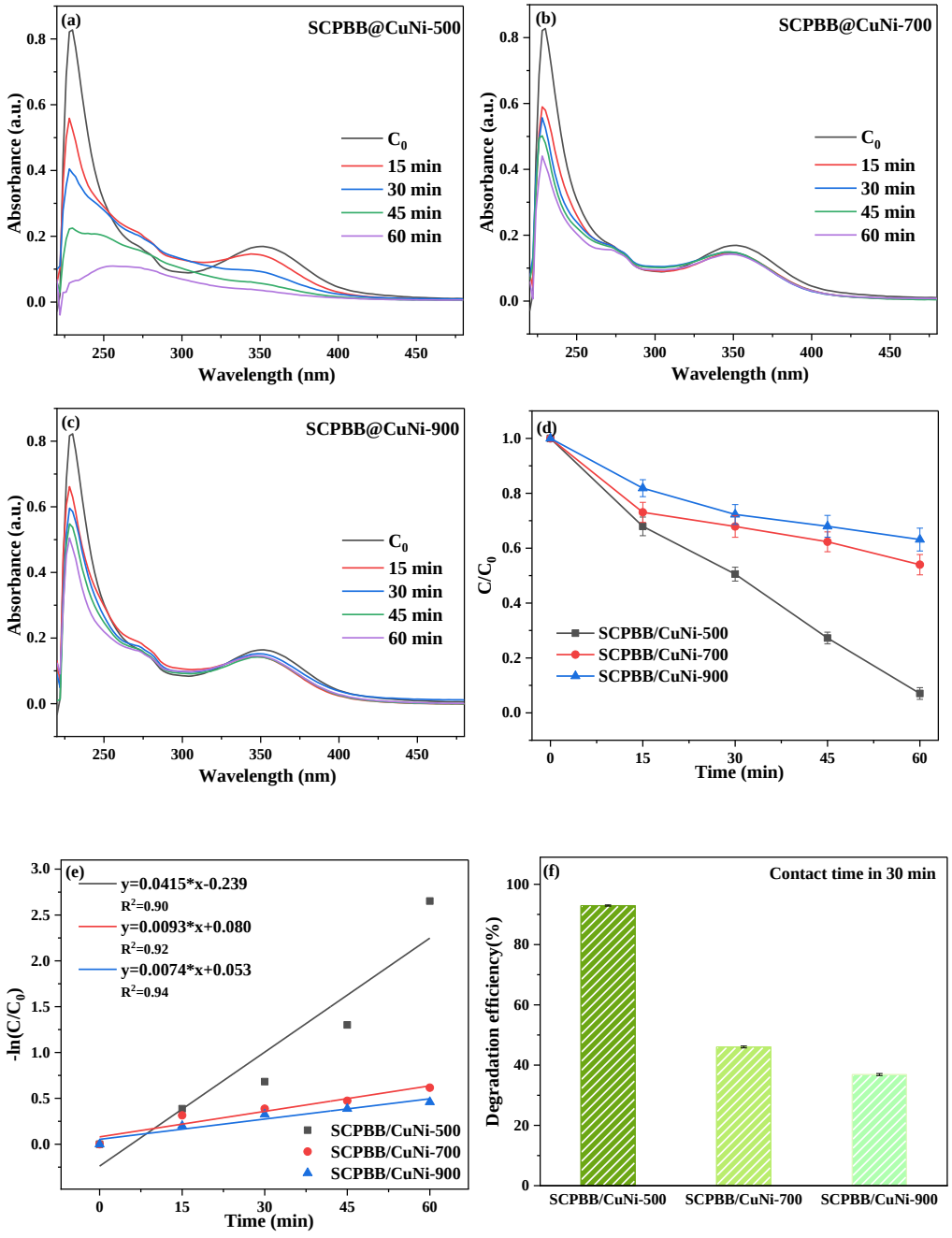

Fig. 9. Removal of Amoxicillin: UV-vis spectra using SCPBB/CuNi-500(a), SCPBB/CuNi-700(b), SCPBB/CuNi-900(c), C/C_0-vs-time plots(d), -ln (C/C_0)-vs-time plot(e), the corresponding removal % in 30 min(f).

Furthermore, the degradation of pharmaceuticals is equally significant in the water pollution context; the biochar catalyst/H_2O_2 system were employed for amoxicillin(AMX) degradation at room temperature under advanced oxidation processes. The experiments revealed that AMX self-degradation with H_2O_2 was negligible in the absence of the catalyst. The addition of SCPBB/CuNi as a H_2O_2 activator proved crucial for AMX degradation. The catalyst amount of 0.25 g/L, the initial concentration of AMX of 20 PPM, resulted in a remarkable catalytic activity to assess the degradation of AMX. Fig. 9a-c illustrate the gradual decrease in the spectra intensity of AMX with increasing catalytic time. Fig. 9d displayed the removal trends of antibiotic, revealing that SCPBB/CuNi catalyst achieved the highest degradation efficiency within 60 minutes. The rate constants, determined from the pseudo-first-order reaction kinetics, were 0.0415 min^{-1}, 0.0093 min^{-1} and 0.0074 min^{-1} for SCPBB/CuNi-500, SCPBB/CuNi-700 and SCPBB/CuNi-900, respectively (Fig. 9e). Correspondingly, Fig. 9g illustrated degradation efficiencies of 93%, 46% and 37% for SCPBB/CuNi-500, SCPBB/CuNi-700 and SCPBB/CuNi-900 within 60 min, highlighting the superior degradation rate of SCPBB/CuNi-500 catalyst.

3.2.3. Removal of methyl-paraben

Methyl paraben(MP) was selected as the model pollutant of pharmaceutical field was studied the catalytic activity and degradation performances of SCPBB/CuNi composites with different pyrolysis temperatures. 250mg/L of catalysts were carried out to removal 20mg/L of MP with H_2O_2(Fig. 10). After 180 min of degradation test, the SCPBB/CuNi-500, -700 and -900 catalysts could degrade MP at room temperature and daylight reached 97%, 77% and 82%, respectively. It is found that the SCPBB/CuNi-500 showed the highest removal efficiency on the degradation of MP, the catalyst could be effectively activate H_2O_2 to generate the oxidation capacity.

Subsequently, the first-order kinetic characteristics reflected that a linear relationship with different temperatures, it is noted that the reaction rates constants were very close during the initial 90 min among all catalyst, after that, SCPBB/CuNi-500 showed the best reaction rate constant compared with other two catalysts.

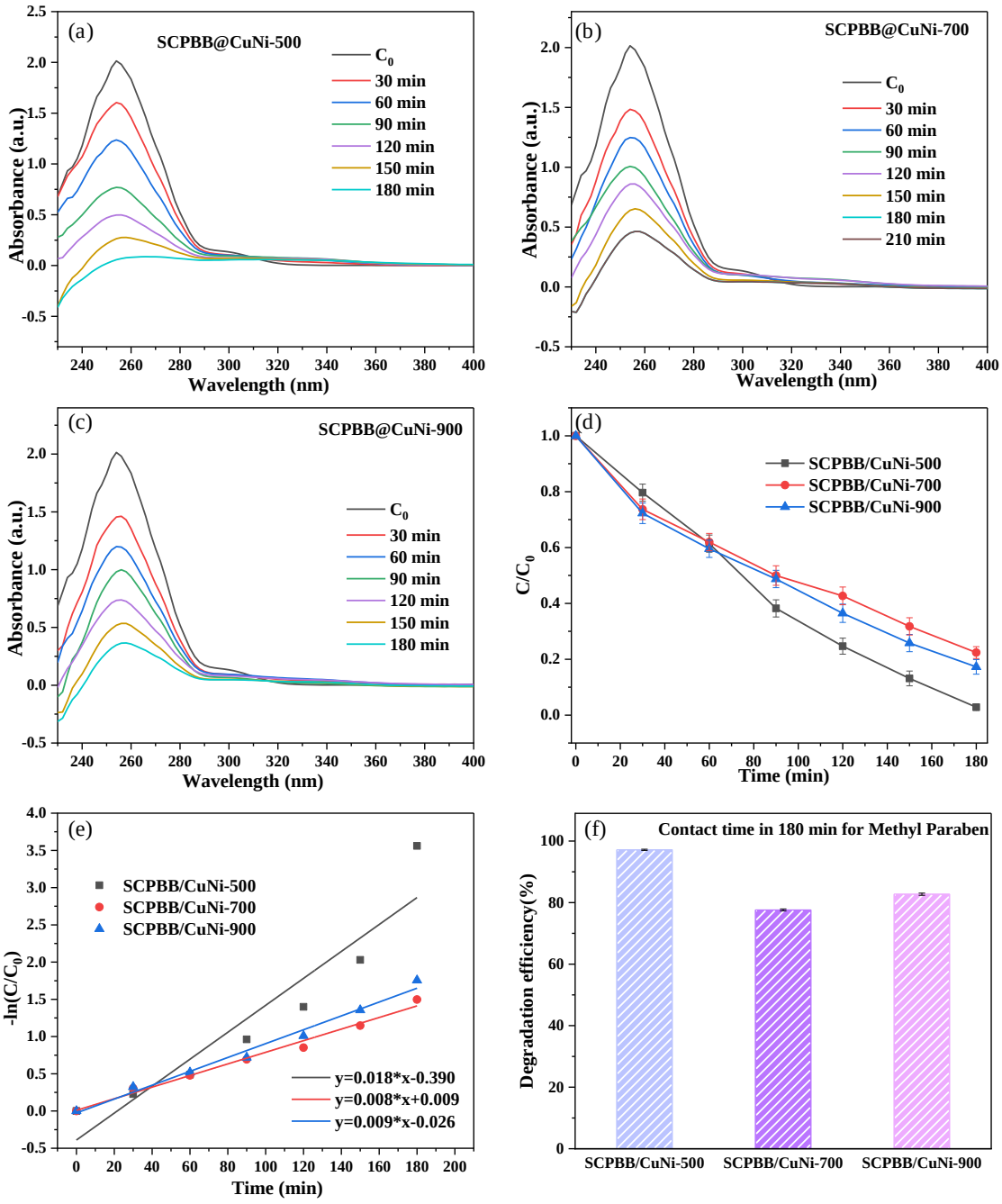

Fig. 10. Removal of Methyl paraben: UV-vis spectra using SCPBB/CuNi-500(a), SCPBB/CuNi-700(b), SCPBB/CuNi-900(c), C/C_0-vs-time plots(d), -ln (C/C_0)-vs-time plot(e), the corresponding removal % in 180 min(f).

As the results mentioned before, SCPBB/CuNi composite showed efficient degradation performance of wastewater containing pollutants from dyes, pharmaceuticals, and personal care products. For the treatment of complex pollutant molecules, the catalytic activity highly dependent on the pyrolysis temperature, with the optimal temperature being 500 °C. Thus, it is noticeable that the pyrolysis temperature plays a crucial role in influencing the catalytic performance of the catalyst. As mentioned before in the XPS section, it is possible that the pyridinic nitrogen type plays an important role as the best catalytic performances were obtained at 500 °C pyrolysis temperature, for which a highest pyridinic nitrogen contribution is obtained. This type of nitrogen is versatile; it has a Lewis donor characteristic and can be protonated-deprotonated. It follows that the pollutant molecule adsorption could be favored on such biochar sites whilst the nanocatalyst cleaves the hydrogen peroxide for further action to degrade the dye or the PPCP.

Moreover, one key feature of the composite catalysts prepared so far, they are highly stable with CuNi nanoparticles tightly bound to the underlying biochar; this we have reported previously [https://doi.org/10.1016/j.envres.2023.116232].

Table 1. The catalytic efficiency of the composites prepared in this work is compared with that of other researches.

Catalyst	Experimental conditions	Contact Time(min)	Degradation (%)	References
Malachite Green				
Nitrogen-doped carbon dots	Catalyst 1 g/L, MG 93 mg/L, room temperature	60	>95	10.1016/j.talanta.2023.125278
mZVI/NGB	Catalyst 0.2 g/L, MG 20 mg/L, H_2O_2 1 mM, pH 5.8	30	>95	10.1016/j.jcis.2024.01.061
$Bi_2O_2CO_3/CuBi_2O_4$	Catalyst 1 g/L, MG 200 mg/L, pH 6, temperature 25 °C, simulated sunlight	180	91.6	10.1016/j.psep.2024.01.097
SCPBB@CuNi	Catalyst 0.25 g/L, H_2O_2 48 mmol/L, MG 20 mg/L, room temperature	30	>99	This work
Amoxicillin				
SCB/Fe_3O_4	Catalyst 0.12 g, AMX 100 mg/L, pH 6, sunlight radiation	240	74.07%	10.1021/acsomega.3c08116

Cu–Fe–FeC_3@NDB	Catalyst 2 g/L, H_2O_2, AMX 100 mg/L,pH 4-8.5, Electrolysis current density 12 mA cm^{-2}	35	> 58%	10.1016/j.cej.2022.134675
CuI/$FePO_4$	Catalyst 1 g/L, AMX 20 mg/L, Osram lamp 400 W	120	~90%	10.1016/j.jallcom.2021.162176
SCPBB@CuNi-500	Catalyst 0.25 g/L, H_2O_2 48 mmol/L, AMX 20 mg/L, room temperature	60	>93%	This work
Methyl paraben				
Ni/Co/CN	Catalyst 0.1 g/L, MP 75 mg/L, LED light 4.2 W	120	~100%	10.1016/j.chemosphere.2023.140680
In_2S_3/WS_2	Catalyst 20 mg, MP 100 mg L^{-1}, Xe lamp 400 W, pH 7	90	95.8 %	10.1016/j.chemosphere.2023.138235
CX/CoFe	Catalyst 25 mg/L, MP 1 mg/L, ultrasound irradiation 25/ 52 W/L, temperature 20°C	60 min	54.6%/100%	10.1016/j.ultsonch.2020.105045
SCPBB@CuNi-500	Catalyst 0.25 g/L, H_2O_2 48 mmol/L, MP 20 mg/L, room temperature	180	>97%	This work

In our case, the SCPBB/CuNi-500, as multipurpose catalyst, is to boost the degradation of malachite green, amoxicillin drug and methyl paraben. Its performances are compared to those of other catalysts reported in the literature (Table 1). Thara et al. [10.1016/j.talanta.2023.125278] degraded 95% of MG within 60 min using nitrogen-doped carbon dots synthesized by microwave method. Sokhansanj et al. [10.1016/j.psep.2024.01.097] reported the degradation MG of 91.6 within 180 min when using $Bi_2O_2CO_3/CuBi_2O_4$ under sunlight radiation. For AMX drug, Zulfiqar et

al. [10.1021/acsomega.3c08116] reported 74.1% degradation using SCB/Fe_3O_4 under sunlight radiation for 240 mins, whereas Beshkar et al. [10.1016/j.jallcom.2021.162176] found 90% degradation under visible light radiation in 120 min using CuI/$FePO_4$ photocatalyst. The degradation of AMX has also been reported using the different Cu–Fe–Fe_3C@NDB electrolysts prepared at the pyrolysis temperatures and the degradation efficiencies under current density 12 mA cm^{-2} were 58.0, 78.1, 99.3, and 97.4% at 500, 600, 700 and 800 °C, respectively [10.1016/j.cej.2022.134675]. It is worth to mention the methyl paraben degradation efficiency reported by Alhamzani et al. [10.1016/j.chemosphere.2023.138235] using In_2S_3/WS_2 heterostructure catalyst (~95.8 % under visible light irradiation, at pH 7, and within 90 min). Zanias et al. [10.1016/j.ultsonch.2020.105045] reported ultrasound irradiation system to form H_2O_2 for the degradation of MP molecule using CX/CoFe; the degradation efficiency was found to be 54.6% for 25 W/L and 100 % for 52 W/L. Comparative studies clearly show that in our case, using SCPBB/CuNi-500 as catalyst with H_2O_2, the diverse degradations of MG, AMX, and MP were demonstrated to complete within 30, 60, and 180 min, respectively, without additional change in temperature, pH, and light irradiation.

3.3 Possible mechanism

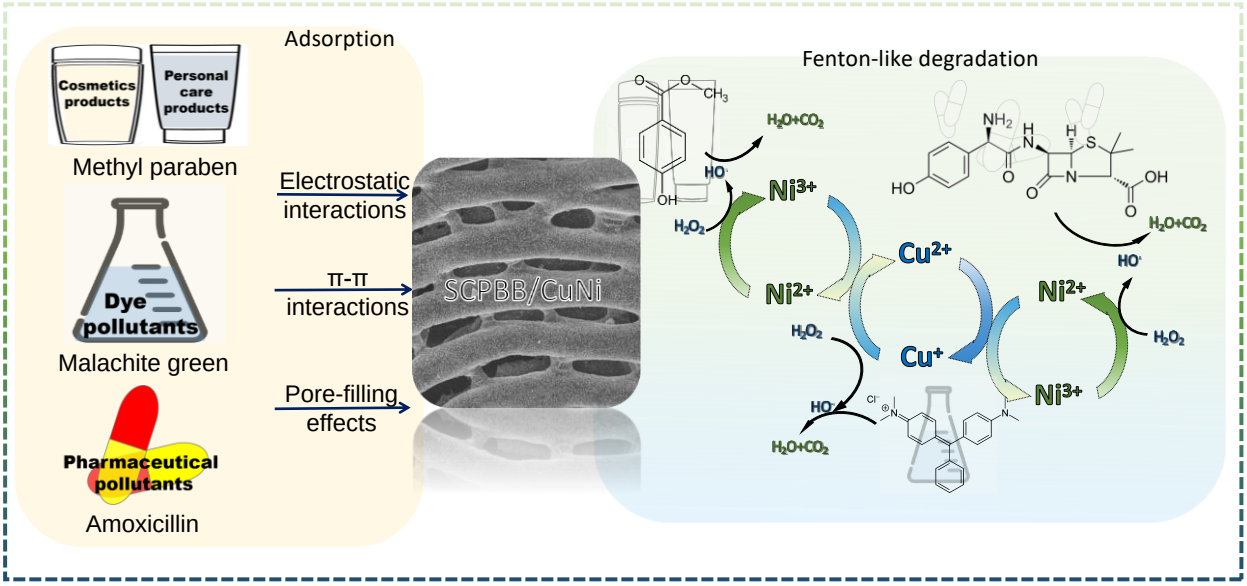

Fig. 11. Reaction mechanism diagram removal organic pollutant using SCPBB/CuNi-500.

According to the experimental findings, the degradation of organic pollutant molecules by the SCPBB/CuNi composite occurs through the synergistic effects of adsorption and Fenton-like reactions, as illustrated in the reaction mechanism diagram shown in Fig. 11. Initially, electrostatic interaction/coordination bonds between the transition metals (i.e., copper and nickel)/functional group on the composite material and organic molecules, leading to adsorption on the surface of SCPBB/CuNi[20]. The aromatic rings in SCPBB form π-π interactions with the aromatic rings of the organic molecules [39]. In addition, BET measurements indicate main mesoporous pore sizes larger than 2.43 nm, indicating that organic molecules adsorbed in the composite material through pore-filling interaction[40].

For the Fenton-like degradation system, it is noteworthy that the transformation and recovery of the metal oxidation states on the catalyst, along with the generation of reactive oxygen species (ROS) from H_2O_2, are closely associated with the degradation of organic contaminants[41-43]. Firstly, Cu^{2+} is reduced to Cu^{+} by decomposition of H_2O_2, because the standard potential (E_0) of $HO_2•/H_2O_2$(+1.44 V) is higher than that of Cu^{2+}/Cu^{+}(+0.159 V) (Eq.1)[21,44]. Subsquently, Cu^{+} and Ni^{2+} on the composite surface gives rise to Cu^{2+} and Ni^{3+} and hydroxyl radicals (·OH) (Eq. 2 and 3). After that, reduced Ni^{3+} to Ni^{2+} by Cu^{+} due to the E_0 of Cu^{2+}/Cu^{+} is lower than that of Ni^{3+}/Ni^{2+} (2.94 V)(Eq. 4)[20]. These indicates that CuNi nanoparticles can form a continuous redox transformation, as both metal ions can undergo recycle on the biochar surface. Ultimately, the reactive hydroxyl radicals (·OH) as the main active species attacks pollutant molecules, degrading them into CO_2

and H_2O (Eq. 5).

$Cu^{2+} + H_2O_2 \rightarrow Cu^{+} + HO_2^{\bullet} + H^{+}$ (1)

$Cu^{+} + H_2O_2 \rightarrow Cu^{2+} + HO^{\bullet} + OH^{-}$ (2)

$Ni^{2+} + H_2O_2 \rightarrow Ni^{3+} + HO^{\bullet} + OH^{-}$ (3)

$Cu^{+} + Ni^{3+} \rightarrow Cu^{2+} + Ni^{2+}$ (4)

Pollutant molecules + $HO^{\bullet} \rightarrow CO_2 + H_2O$ (5)

In order to further illustrate the influence of light on the whole process, catalytic degradation tests using SCPBB/CuNi were conducted under visible light conditions in comparison to dark conditions. Taking AMX molecules as an example, it was observed that there was no significant difference in AMX removal efficiency between dark and visible light conditions, indicating that the photocatalytic effect of SCPBB/CuNi under AOPs can be negligible.

4. Conclusion

SCPBB and SCPBB/CuNi composites were prepared by the pyrolysis and wet impregnation/pyrolysis approach in the 500 to 900 °C temperature range. XRD data confirmed CuNi as alloy loaded on biochar-based samples. SEM images indicated that the sized of CuNi nanoparticles with spherical shape dispersed on biochar surface increased with increasing the pyrolysis temperature. FT-IR ATR and Raman spectra showed that SCPBB/CuNi composite materials retain the surface functional groups and carbon structure present in the SCPBB material. TGA indicates that the introduction of CuNi nanoparticles enhances the thermal stability of the SCPBB supports. Subsequently, under indoor visible light and room temperature conditions, the catalytic degradation were carried out with catalysts/AOPs system toward dyes, pharmaceuticals and personal care products. Regarding Methyl-paraben, the degradation rate of SCPBB/CuNi remained above 77 %. Malachite Green can be completely degraded with SCPBB/CuNi samples in 30 mins. The degradation efficiency of Amoxicilline in the presence of SCPBB/CuNi-500, -700, and -900 were 93%, 46%, and 37%, respectively. Thus, SCPBB/CuNi prepared by optimal pyrolysis temperature 500 °C may serve as a potential candidate material for mitigating toxic organic pollutants into the aquatic environment. Slow pyrolysis is an interesting process because it gives a high yield of solid biochar support over the two other main products (gas and bio-oil). The direct wet impregnation employing nickel catalyst precursor ensures obtaing supported nanocatalysts over porous biochar structure from the pulp of sugarcane. Yet, it remains tedious to anticipate which biomass will enable obtaining a porous structure; this requires a full comprehensive study. Moreover, we tentatively correlated the efficient catalysis with the pyrolysis temperature of 500 °C which yielded the highest relative concentration of pyridinic centres. However, this point

merits also a comprehensive study of the nitrogen centres which could be obtained from the natural initial biomass, but also by doping the biomass with a nitrogen-containing species such as urea.

Beyond the firm results and open questions, SCPBB/CuNi is indisputably a potential candidate material to mitigate toxic organic emerging contaminants in aquatic environments. It is a low-coast and sustainable composite material; it helps to address SDG6 (clean water and sanitation) and SDG14 (life below water).

Acknowledgements

M. Tang is indebted to the China Scholarship Council for the provision of PhD scholarship (No, 202008310221). Wallonie Bruxelles International (WBI) is acknowledged for the provision of a grant to A.K. Bhakta through "Bourse WBI Excellence World" (No. Imputation 101386, Article Budgétaire 13 33.01.00.07). All authors would like to thank A. Chevillot-Biraud, P. Decorse, S. Lau-Truong, and S. Novak (experimental officers at ITODYS lab) for their assistance with TGA, XPS, Raman and XRD studies. We are grateful to Prof. A. M. Khalil for the gift of sugarcane bagasse sample.

[1] M. Jayakumar, A.S. Hamda, L.D. Abo, B.J. Daba, S. Venkatesa Prabhu, M. Rangaraju, A. Jabesa, S. Periyasamy, S. Suresh, G. Baskar, Comprehensive review on lignocellulosic biomass derived biochar production, characterization, utilization and applications, *Chemosphere, 345* (2023) 140515-140515. https://doi.org/10.1016/j.chemosphere.2023.140515.

[2] X. Xu, Y. Wu, X. Wu, Y. Sun, Z. Huang, H. Li, Z. Wu, X. Zhang, X. Qin, Y. Zhang, J. Deng, J. Huang, Effect of physicochemical properties of biochar from different feedstock on remediation of heavy metal contaminated soil in mining area, *Surf. Interfaces, 32* (2022). https://doi.org/10.1016/j.surfin.2022.102058.

[3] L. Li, D. Zou, Z. Xiao, X. Zeng, L. Zhang, L. Jiang, A. Wang, D. Ge, G. Zhang, F. Liu, Biochar as a sorbent for emerging contaminants enables improvements in waste management and sustainable resource use, *J. Clean. Prod., 210* (2019) 1324-1342. https://doi.org/10.1016/j.jclepro.2018.11.087.

[4] R.K. Sathish Kumar, R. Sasikumar, T. Dhilipkumar, Exploiting agro-waste for cleaner production: A review focusing on biofuel generation, bio-composite production, and environmental considerations, *J. Clean. Prod.,* (2024) 140536-140536. https://doi.org/10.1016/j.jclepro.2023.140536.

[5] Alokika, Anu, A. Kumar, V. Kumar, B. Singh, Cellulosic and hemicellulosic fractions of sugarcane bagasse: Potential, challenges and future perspective, *Int. J. Biol. Macromol., 169* (2021) 564-582. https://doi.org/10.1016/j.ijbiomac.2020.12.175.

[6] M.K. Zafeer, R.A. Menezes, H. Venkatachalam, K.S. Bhat, Sugarcane bagasse-based biochar and its potential applications: a review, *Emergent Materials, 7* (2024) 133-161. https://doi.org/10.1007/s42247-023-00603-y.

[7] M. Stylianou, T. Lai, S. Bennici, P. Dutournie, L. Limousy, A. Agapiou, I. Papamichael, B. Khiari, M. Jeguirim, A.A. Zorpas, Tomato waste biochar in the framework of circular economy, *Sci. Total Environ., 871* (2023). https://doi.org/10.1016/j.scitotenv.2023.161959.

[8] K. Weber, P. Quicker, Properties of biochar, *Fuel, 217* (2018) 240-261. https://doi.org/10.1016/j.fuel.2017.12.054.

[9] M. Tang, Y. Snoussi, A.K. Bhakta, M. El Garah, A.M. Khalil, S. Ammar, M.M. Chehimi, Unusual, hierarchically structured composite of sugarcane pulp bagasse biochar loaded with Cu/Ni bimetallic nanoparticles for dye removal, *Environ. Res., 232* (2023). https://doi.org/10.1016/j.envres.2023.116232.

[10] L. Boubkr, A.K. Bhakta, Y. Snoussi, C.M. Da Silva, L. Michely, M. Jouini, S. Ammar, M.M. Chehimi, Highly Active Ag-Cu Nanocrystal Catalyst-Coated Brewer's Spent Grain Biochar for the Mineralization of Methyl Orange and Methylene Blue Dye Mixture, *CATALYSTS, 12* (2022). https://doi.org/10.3390/catal12111475.

[11] Y. Snoussi, M. El Garah, A.M. Khalil, S. Ammar, M.M. Chehimi, Immobilization of biogenic silver-copper nanoparticles over arylated biochar from sugarcane bagasse: Method and catalytic performance, *Appl. Organomet. Chem., 36* (2022). https://doi.org/10.1002/aoc.6885.

[12] G. Pan, Z. Sun, Cu-doped g-C₃N₄ catalyst with stable Cu⁰ and Cu⁺ for enhanced amoxicillin degradation by heterogeneous electro-Fenton process at neutral pH, *Chemosphere, 283* (2021). https://doi.org/10.1016/j.chemosphere.2021.131257.

[13] Z. Wu, Y.-y. Gu, S. Xin, L. Lu, Z. Huang, M. Li, Y. Cui, R. Fu, S. Wang, Cu_xNi_yCo-LDH nanosheets on graphene oxide: An efficient and stable Fenton-like catalyst for dual-mechanism degradation of tetracycline, *Chem. Eng. J., 434* (2022). https://doi.org/10.1016/j.cej.2022.134574.

[14] J. Omiri, Y. Snoussi, A.K. Bhakta, S. Truong, S. Ammar, A.M. Khalil, M. Jouini, M.M. Chehimi, Citric-Acid-Assisted Preparation of Biochar Loaded with Copper/Nickel Bimetallic Nanoparticles for Dye Degradation, *Colloids And Interfaces, 6* (2022). https://doi.org/10.3390/colloids6020018.

[15] H. Bayoka, Y. Snoussi, A.K. Bhakta, M. El Garah, A.M. Khalil, M. Jouini, S. Ammar, M.M. Chehimi, Evidencing the synergistic effects of carbonization temperature, surface composition and structural properties on the catalytic activity of biochar/ bimetallic composite, *J. Anal. Appl. Pyrolysis, 173* (2023). https://doi.org/10.1016/j.jaap.2023.106069.

[16] M.A.-E.A. Anekwe Jennifer Ebele, Stuart Harrad Pharmaceuticals and personal care products (PPCPs) in the freshwater aquatic environment, *Emerg. Contam., 3* (2017) 1-16. https://doi.org/10.1016/j.emcon.2016.12.004.

[17] S. Feijoo, X. Yu, M. Kamali, L. Appels, R. Dewil, Generation of oxidative radicals by advanced oxidation processes (AOPs) in wastewater treatment: a mechanistic, environmental and economic review, *Rev. Environ. Sci. Bio., 22* (2023) 205-248. https://doi.org/10.1007/s11157-023-09645-4.

[18] T.S. Rad, E.S. Yazici, A. Khataee, E. Gengec, M. Kobya, Ultrasound-assisted photocatalytic decomposition of rifadin with biochar and CNT-based NiCr layered double hydroxides, *Surf. Interfaces, 36* (2023). https://doi.org/10.1016/j.surfin.2022.102628.

[19] Z. Zhao, Y. Ren, S. Qi, Z. Ning, X. Wang, W. Dong, H. Wang, Enhanced removal of Ni-EDTA by three-dimensional electro-Fenton process using Fe-N-doped biochar as catalytic particle electrodes, *Chem. Eng. J., 471* (2023). https://doi.org/10.1016/j.cej.2023.144717.

[20] A.S. Eltaweil, N.M. Gaber, G.M. El-Subruiti, A.M. Omer, Dandelion-like Cu-Ni LDH-decorated biochar/aminated chitosan composite for boosting Fenton-like degradation of doxycycline: Insights into performance and mechanism, *J. Mol. Liq., 394* (2024). https://doi.org/10.1016/j.molliq.2023.123716.

[21] Y. Liu, J. Wang, Multivalent metal catalysts in Fenton/Fenton-like oxidation system: A critical review, *Chem. Eng. J., 466* (2023). https://doi.org/10.1016/j.cej.2023.143147.

[22] H. Liu, M. Ye, X. Dong, Z. Ren, S. Long, E. Lichtfouse, Removal of humic substances by the synergistic effect of biochar adsorption and activation of persulfate, *J. Water Process Eng., 44* (2021). https://doi.org/10.1016/j.jwpe.2021.102428.

[23] M. Xu, C. Sheng, Influences of the Heat-Treatment Temperature and Inorganic Matter on Combustion Characteristics of Cornstalk Biochars, *Energy & Fuels, 26* (2012) 209-218. https://doi.org/10.1021/ef2011657.

[24] D. Yang, C. Sararuk, K. Suzuki, Z. Li, C. Li, Effect of calcination temperature on the catalytic activity of VPO for aldol condensation of acetic acid and formalin, *Chem. Eng. J., 300* (2016) 160-168. https://doi.org/10.1016/j.cej.2016.04.107.

[25] A. Allahbakhsh, Nitrogen-doped graphene quantum dots hydrogels for highly efficient solar steam generation, *Desalination, 517* (2021). https://doi.org/10.1016/j.desal.2021.115264.

[26] B. Khiari, A. Ibn Ferjani, A.A. Azzaz, S. Jellali, L. Limousy, M. Jeguirim, Thermal conversion of flax shives through slow pyrolysis process: in-depth biochar characterization and future potential use, *Biomass Convers. Biorefin., 11* (2021) 325-337. https://doi.org/10.1007/s13399-020-00641-0.

[27] M. Xu, H. Hu, Y. Yang, Y. Huang, K. Xie, H. Liu, X. Li, H. Yao, I. Naruse, A deep insight into carbon conversion during Zhundong coal molten salt gasification, *Fuel, 220* (2018) 890-897. https://doi.org/10.1016/j.fuel.2017.12.051.

[28] C. Guizani, K. Haddad, L. Limousy, M. Jeguirim, New insights on the structural evolution of biomass char upon pyrolysis as revealed by the Raman spectroscopy and elemental analysis, *Carbon, 119* (2017) 519-521. https://doi.org/10.1016/j.carbon.2017.04.078.

[29] K. Zeng, R. Li, D.P. Minh, E. Weiss-Hortala, A. Nzihou, D. Zhong, G. Flamant, Characterization of char generated from solar pyrolysis of heavy metal contaminated biomass, *Energy, 206* (2020). https://doi.org/10.1016/j.energy.2020.118128.

[30] C. Schneider, S. Walker, A. Phounglamcheik, K. Umeki, T. Kolb, Effect of calcium dispersion and graphitization during high-temperature pyrolysis of beech wood char on the gasification rate with CO₂, *Fuel, 283* (2021). https://doi.org/10.1016/j.fuel.2020.118826.

[31] Q. Yan, C. Wan, J. Liu, J. Gao, F. Yu, J. Zhang, Z. Cai, Iron nanoparticles in situ encapsulated in biochar-based carbon as an effective catalyst for the conversion of biomass-derived syngas to liquid hydrocarbons, *Green Chem., 15* (2013) 1631-1640. https://doi.org/10.1039/c3gc37107g.

[32] H. Zhang, C. Chen, E.M. Gray, S.E. Boyd, Effect of feedstock and pyrolysis temperature on properties of biochar governing end use efficacy, *Biomass & Bioenergy, 105* (2017) 136-146.

https://doi.org/10.1016/j.biombioe.2017.06.024.

[33] R.R. Domingues, P.F. Trugilho, C.A. Silva, I.C.N.A. de Melo, L.C.A. Melo, Z.M. Magriotis, M.A. Sanchez-Monedero, Properties of biochar derived from wood and high-nutrient biomasses with the aim of agronomic and environmental benefits, *Plos One, 12* (2017). https://doi.org/10.1371/journal.pone.0176884.

[34] J. Kaewyai, P. Noophan, S.G. Cruz, S. Okabe, Influence of biochar derived from sugarcane bagasse at different carbonization temperatures on anammox granular formation, *Int. Biodeterior. Biodegrad., 185* (2023). https://doi.org/10.1016/j.ibiod.2023.105678.

[35] R.K. Singh, D. Pandey, T. Patil, A.N. Sawarkar, Pyrolysis of banana leaves biomass: Physico-chemical characterization, thermal decomposition behavior, kinetic and thermodynamic analyses, *Bioresour. Technol., 310* (2020). https://doi.org/10.1016/j.biortech.2020.123464.

[36] M. Garcìa-Pèrez, A. Chaala, J. Yang, C. Roy, Co-pyrolysis of sugarcane bagasse with petroleum residue.: Part I:: thermogravimetric analysis, *Fuel, 80* (2001) 1245-1258. https://doi.org/10.1016/s0016-2361(00)00215-5.

[37] L.C. Morais, A.A.D. Maia, M.E.G. Guandique, A.H. Rosa, Pyrolysis and combustion of sugarcane bagasse, *J. Therm. Anal. Calorim., 129* (2017) 1813-1822. https://doi.org/10.1007/s10973-017-6329-x.

[38] Saruchi, V. Kumar, A.A. Ghfar, S. Pandey, Microwave Synthesize Karaya Gum-Cu, Ni Nanoparticles Based Bionanocomposite as an Adsorbent for Malachite Green Dye: Kinetics and Thermodynamics, *Front. Mater., 9* (2022). https://doi.org/10.3389/fmats.2022.827314.

[39] H. Chakhtouna, H. Benzeid, N. Zari, A.e.K. Qaiss, R. Bouhfid, Functional CoFe₂O₄-modified biochar derived from banana pseudostem as an efficient adsorbent for the removal of amoxicillin from water, *Sep. Purif. Technol., 266* (2021). https://doi.org/10.1016/j.seppur.2021.118592.

[40] Y. Chen, M. Hassan, M. Nuruzzaman, H. Zhang, R. Naidu, Y. Liu, L. Wang, Iron-modified biochar derived from sugarcane bagasse for adequate removal of aqueous imidacloprid: sorption mechanism study, *Environ. Sci. Pollut. Res., 30* (2023) 4754-4768. https://doi.org/10.1007/s11356-022-22357-6.

[41] A.D. Bokare, W. Choi, Review of iron-free Fenton-like systems for activating H₂O₂ in advanced oxidation processes, *J. Hazard. Mater., 275* (2014) 121-135. https://doi.org/10.1016/j.jhazmat.2014.04.054.

[42] Z. Wang, Y. Du, P. Zhou, Z. Xiong, C. He, Y. Liu, H. Zhang, G. Yao, B. Lai, Strategies based on electron donors to accelerate Fe(III)/Fe(II) cycle in Fenton or Fenton-like processes, *Chem. Eng. J., 454* (2023). https://doi.org/10.1016/j.cej.2022.140096.

[43] G.A. Kifle, Y. Huang, M. Xiang, W. Wang, C. Wang, C. Li, H. Li, Heterogeneous activation of peroxygens by iron-based bimetallic nanostructures for the efficient remediation of contaminated water. A review, *Chem. Eng. J., 442* (2022). https://doi.org/10.1016/j.cej.2022.136187.

[44] X. Liu, Y. Zhai, G. Liu, X. Liu, B. Wang, Z. Wang, Y. Zhu, Y. Fan, H. Shi, M. Xu, Mechanistic insights into enhanced waste activated sludge dewaterability with Cu(II) and Cu(II)/H₂O₂ treatment: Radical and non-radical pathway, *Chemosphere, 288* (2022). https://doi.org/10.1016/j.chemosphere.2021.132549.